Schottky Photodiodes Based on Mid-Wavelength Infrared Intraband Colloidal Quantum Dots – Surface Ligand and Metal Contact Studies

Mohammad M. Al Mahfuz[a], *Junsung Park*[a], *Rock Huebner*[b], *Sunghwan Lee*[c], *Dong-Kyun Ko*[a,*]

[a] Department of Electrical and Computer Engineering, New Jersey Institute of Technology,

Newark, NJ 07102, United States

[b] Department of Mechanical and Industrial Engineering, New Jersey Institute of Technology,

Newark, NJ 07102, United States

[c] School of Engineering Technology, Purdue University, West Lafayette, IN 47907, United

States

* Corresponding author. E-mail address: dkko@njit.edu

KEYWORDS: Schottky diode, Intraband, Silver selenide, Colloidal quantum dots, Mid-wavelength infrared

Abstract: There is an emergent need for low-cost, uncooled detectors operating in the mid-wavelength infrared. Here, we report the first Schottky junction diode that utilizes intraband Ag_2Se colloidal quantum dots as mid-wavelength infrared absorbers. These inexpensive, solution-processed Schottky devices exhibit orders-of-magnitude suppression of dark current compared to the photoconductors, while providing a greater fabrication simplicity compared to the barrier or p-n heterojunction devices. We highlight our findings on the role of the capping ligand in the detector performance parameters and discuss our metal contact studies to form rectifying junctions to the colloidal quantum dot films. The optimized Schottky devices show a favorable infrared responsivity of 0.1 A/W and an uncooled specific detectivity of 10^7 Jones. We also identify the present limitation of the device (1/f noise) and discuss potential paths toward future improvements.

INTRODUCTION

Materials absorb and emit thermal energies at different rates hence a region of interest whose temperature appears to be uniform is made up of a mosaic of different temperatures. Thermal infrared sensors play an important role in offering this “heat signature” of natural, man-made, and biological objects with applications ranging from military surveillance, astronomy, environmental monitoring, and industrial processing control to medical diagnostics. The current market for high performance sensors is dominated by III-V superlattice, InSb, and HgCdTe devices in the mid-wavelength infrared (MWIR = 3 – 5 μm) and long-wavelength infrared (LWIR = 9 – 12 μm) spectral regions,-despite their high cost and requirement for cryogenic cooling [REF][1, 2]. On the other hand, the demands for low-cost and uncooled options are entirely met by microbolometers, which perform well in the LWIR but poorly in the MWIR due to low responsivity and slow speed [REF] [3]. A significant effort is on the way to fill in this MWIR technology gap. While high operating temperature (HOT) infrared detectors based on epitaxial materials can significantly lower the cost by removing the need for cryogenic coolers, the overall price is still plagued by the high cost of equipment – especially molecular beam epitaxy (MBE), expensive substrates, and slow film growth [REF] [4]. Recently, nanotechnology-enabled devices, including 2D materials such as graphene [REF] [5, 8] as well as colloidal quantum dots (CQDs) [REF] [9–13], have provided a potential path toward low-cost, uncooled MWIR sensing. In particular, CQDs – which is the only available solution-processed materials option in the MWIR – are synthesized using facile benchtop chemistry, and the photoresponsive film can be deposited directly on top of silicon read-out integrated circuits (ROICs) at the wafer scale. This enables the monolithic fabrication of focal plane arrays (FPAs) without the complexity of hybridization (indium bump bonding) required in traditional epitaxial technologies, thereby further reducing the manufacturing cost [REF] [14].

Intraband CQDs are an emerging member of the semiconductor CQD materials family which are doped up to the first quantum confined energy levels ($1S_e$) and utilize the optical transitions between $1S_e$ and the second ($1P_e$) quantum confined energy levels. It has been studied that the Auger recombination process, which is a major obstacle that prevents narrow bandgap semiconductor detectors from reaching high sensitivity without cooling, is dramatically suppressed due to the sparse distribution of density of states [REF] [15]. This can allow high sensitivity MWIR photodetection at elevated temperatures, an exemplary example being lead salt (PbSe) detectors [REF] [16]. Ag_2Se intraband CQDs are a non-toxic alternative to HgSe CQDs, which have been demonstrated as a photoconductive barrier, and p-n heterojunction diode devices operating at room temperature [REF] [17–19]. In this work, we demonstrate MWIR Schottky photodiodes based on Ag_2Se CQDs which show reduced dark current and noise ~~than~~ compared to those of the photoconductors and allow simpler device fabrication compared to the barrier devices or p-n heterojunction diodes. We also report our findings on the device performance as a function of varying CQD surface ligands and the contact metallization studies.

RESULTS AND DISCUSSION

The heavily-doped nature of Ag_2Se intraband CQDs presents difficulties in realizing a Schottky barrier with metals because it will electrically form a tunneling contact (Ohmic). In our previous study [REF] [19], we proposed a binary CQD approach to overcome this issue and a similar approach is utilized here. Specifically, we form a binary mixture of intraband Ag_2Se CQDs and intrinsic PbS CQDs to reduce the overall carrier concentration in the film where the transport of ground state electrons and holes are blocked due to the energetic position of the Ag_2Se CQDs with respect to PbS CQDs (see Supporting Information S1). The transport of photoexcited electrons in the Ag_2Se CQDs, on the other hand, remains unimpeded, thereby allowing the generation of photocurrents. First, to prepare the CQD samples, average sizes of 3 nm PbS and 5.5 nm Ag_2Se CQDs were synthesized following the procedure reported in the literature (see Figure 1(a) and 1(b)) [REF][18]. The optical absorption of CQDs was obtained using Fourier transform infrared (FTIR), as shown in Figure 1(c) and 1(d). A broad absorption peak around 3 – 6 μm shown in Figure 1(c) arises from the intraband absorption Ag_2Se CQDs. Figure 1(d) shows the FTIR spectrum of PbS CQDs, which shows an absence of optical absorption in the MWIR. Sharp peaks around 3.4 μm arise from the vibrational signatures of C-H. Using these two types of CQDs, we have prepared the optimized CQD mixture solution sample corresponding to 1:100 (1 Ag_2Se CQDs out of 100 PbS CQDs, see Supporting Information S2 for details).

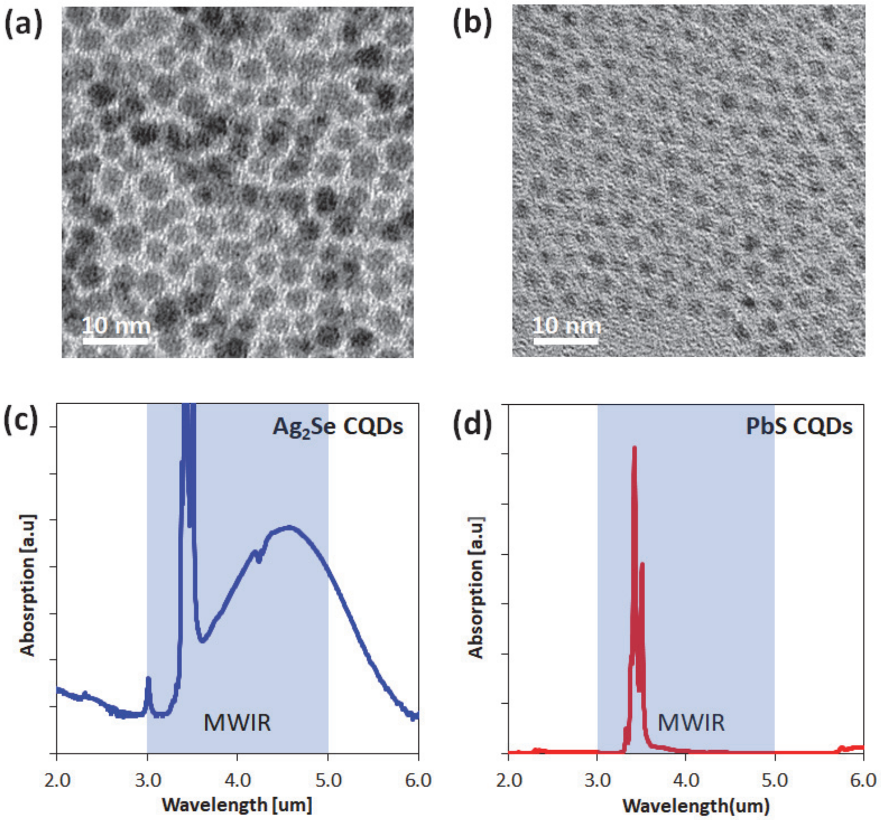

Figure 1. Optical absorption of (a) Ag_2Se CQD and (b) PbS CQD obtained using FTIR measurement. Sharp peaks around 3.4 μm arise from the vibrational signatures of C-H.

The performance of any CQD-based device is known to be highly sensitive to the surface capping ligands. Hence CQD ligand studies were conducted prior to Schottky device studies. The type of ligands investigated are 1,2-ethandithiol (EDT) [REF] [20, 21], 1,3-benzenedithiol (BDT) [REF] [22, 23], 3-mercaptopropionic acid (MPA) [REF] [24, 25], ammonium thiocyanate (SCN) [REF] [26], and tetrabutylammonium iodide (TBAI) [REF] [27]. EDT and BDT serve as standard, compact organic ligands and MPA, SCN, and TBAI were selected due to their reports of high photodetector, solar cell, and transistor performances.

To identify the best performing CQD ligands, we have fabricated vertically-stacked devices to measure two key detector performance parameters: MWIR responsivity and dark resistivity. First, to fabricate the device, a Cr/Au bottom contact is formed on a glass substrate using a shadow mask and thermal evaporation. Then, a total of 8 layers of binary CQD film (~ 120 nm) is deposited using a layer-by-layer spin-coating and ligand-exchange method. The device is completed with a 70 nm top contact Au layer deposited using a shadow mask and thermal evaporation. A device schematic is shown in Figure 2(a). The infrared responsivity of the device was characterized using a lock-in technique with a calibrated blackbody illuminated through a 4.5 μm bandpass filter serving as a radiation source. A series of identical devices were fabricated, except the QD films were ligand-exchanged with various ligands. During measurements, it was noted that the devices made from different ligands have different maximum biases that can be applied; exceeding the maximum bias leads to irreversible degradation of the device. Hence, a low-bias of 0.9 V was used for all devices for responsivity comparison. Figure 2(b) and 2(c) show the device responsivity and dark resistivity, respectively.

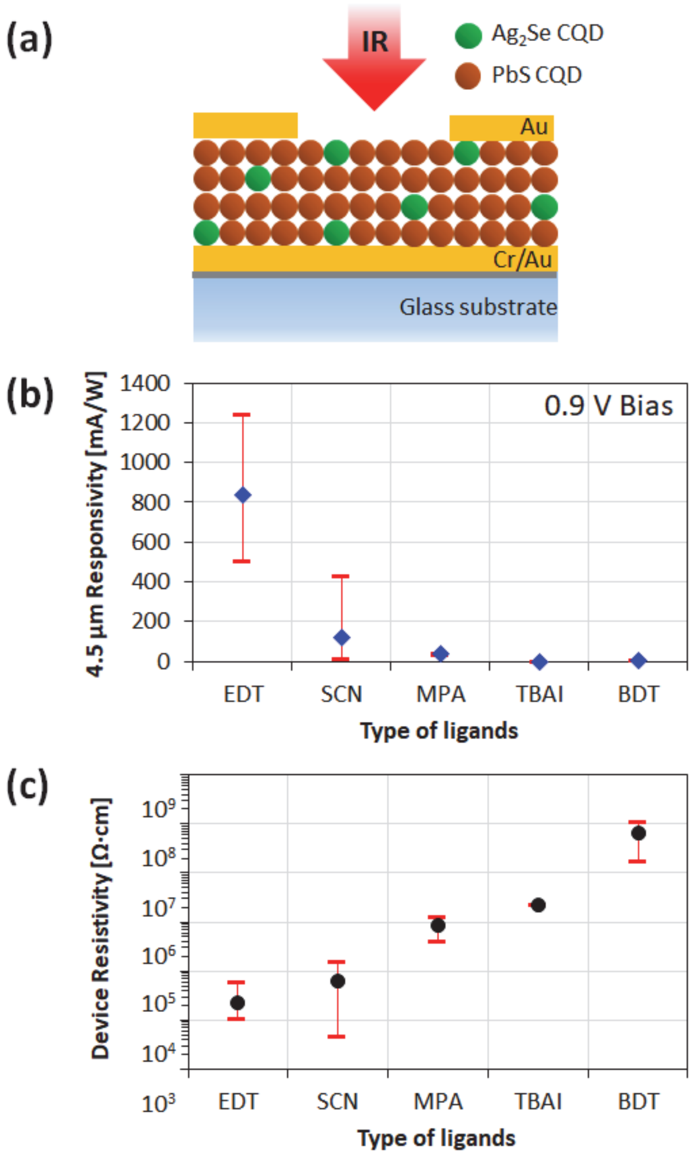

Figure 2. (a) Device schematic of upward-looking, vertically-stacked binary CQD device, (b) plot of 4.5 µm peak responsivity with varying ligands used for CQD film ligand-exchange, and (c) plot of device dark resistivity with varying ligands.

The analysis of the Figure 2 data reveals a trend: for the devices with higher electrical conductivities (lower resistivity), higher responsivities are observed, except for the TBAI devices which showed zero photoresponse at 0.9 V. This can be understood based on the relationship that both the magnitude of dark current and the photocurrent is proportional to the carrier mobility[REFS]. The trend observed here points to the fact that the predominant effect of the ligand-exchange is the change in the carrier mobility of the CQD film. While ligand-exchange can induce changes in the carrier lifetime due to improved/degraded surface defect passivation, the changes are typically small (less than 3-times [7, 11, 12]) [25, 28, 29], compared to the orders of magnitude difference observed in Figure 2 (b) and (c). The size of the ligand determines the interparticle distance and the carrier mobility (μ) of the CQD film has an exponential dependence on the inverse of interparticle distance, given by

$$\mu = \mu_0 \exp(-\mathrm{\beta d}) \exp\left(-\frac{\Delta \mathrm{E}}{\mathrm{kT}}\right)$$

where, μ_0 is the mobility prefactor, β is the tunneling decay constant, d is the interparticle distance, ΔE is the transport energy level variation, k is the Boltzmann constant, and T is the temperature. The order of ligand size studied here is: TBAI (I^- atomic ligand) < SCN (inorganic SCN^- ligand) < EDT (C2-SH) ≤ MPA (C2-COOH) < BDT (most bulky in size) [refs]. While EDT and MPA have the same C2 chain (two carbon backbones), MPA has carboxylic acid on the other end giving rise to **a** different surface binding configuration and this might be the reason for the larger interparticle distance observed in this binary CQD study. With the exception of TBAI and SCN, the device resistivity follows the ligand size trend (EDT < MPA < BDT), as shown in Figure 3(a). The exception of TBAI and SCN occurs due to Schottky contact formation (see Figure 3(b) and Supporting Information S3). EDT, MPA, and BDT form Ohmic or quasi-Ohmic contacts while TBAI and SCN form Schottky contacts to the Au metal electrodes, therefore showing higher-than-anticipated device resistivity. The energetic position of the conduction and valence level of CQDs has been reported previously to vary with the type of surface ligands [REF][30]. The report is consistent with the results obtained here that TBAI and SCN have deeper lying energy levels compared to EDT and MPA (as much as 0.5 eV), thereby forming a Schottky barrier for holes in contact with Au. If the Schottky contacts are formed both at the top and bottom of the CQD film, this would create a back-to-back diode (one diode in opposite polarity to the other). However, Figure 3(b) shows the typical characteristics of a single rectifying diode, indicating that the metal-CQD contact formed at the bottom and the CQD-metal contact formed at the top are different, despite using identical metal material. This arises from the fact that, for the bottom contact, CQDs are mildly solution-deposited on top of metal electrode whereas, for the top contacts, metals are thermally deposited on CQD film; during metal evaporation, the underlying CQD film may be damaged creating defects. This would lead to Fermi level pinning, thereby creating an Ohmic contact irrespective of the type of metal deposited. Device resistivity data shown in Figure 2(c) was extracted from the reverse (negative) bias region, as this region is typically used for the operation photodetector, due to the low dark current.

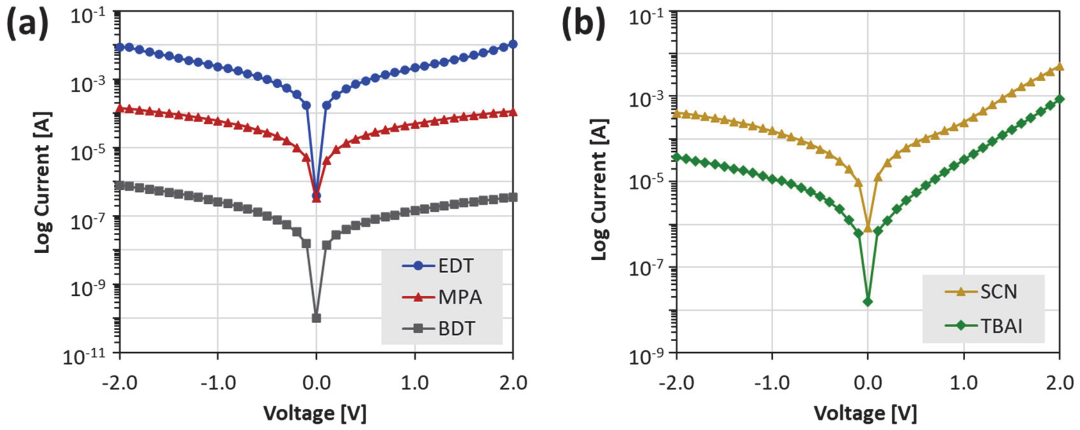

Figure 3. Current-voltage (I-V) characteristics of (a) various organic and (b) inorganic ligands investigated in this study plotted on a logarithmic current scale.

Overall, in terms of determining the optimum ligand, EDT was identified to show the highest infrared responsivity. However, it was noted the EDT devices suffer from the high dark current. The dark current typically determines the magnitude of current noise and it is a major limiting factor for achieving high specific detectivity. As discussed previously, the fact that dark resistivity and responsivity ~~is~~ are interrelated through carrier mobility makes it challenging to maximize the detector sensitivity by modifying the material properties (binary mixture ratios and ligands) alone. Thus, to further improve the detector performance, modification of the device structure is sought. Specifically, since the primary source of dark current in a photoconductive device is the majority carrier drift current, the formation of a Schottky contact barrier will block the flow of majority carriers, thereby significantly reducing the dark current. To fabricate this Schottky diode device, every processing parameter was kept identical except that the Au bottom contact (work function = 5.2 eV) was replaced with low work function Al (work function = 4.1 eV). Based on the lesson learned from the previous ligand optimization study, a Schottky contact was formed at the bottom electrode instead of the top which may create Fermi pinning. Figure 4(a) shows current-voltage (I-V) characteristics comparison of a photoconductor (Au-EDT CQD-Au device) and a Schottky diode (Al-EDT CQD-Au device). A strong rectifying characteristic with an on/off ratio of 2.1×10^{2} (± 2V) was observed due to the Al-binary CQD Schottky barrier formation. Compared to the photoconductor, the Schottky diode exhibits three orders of magnitude reduction in the dark current (under reverse bias) while the magnitude of the 4.5 um peak responsivity (Figure 4(c)) was only reduced by approximately 6-times. This results in about two orders of magnitude increase in the sensitivity ratio (SR), defined as SR = I_{photo}/I_{dark}, from 2.4×10^{-4} (Photoconductor) to 3.6×10^{-2} (Schottky). This EDT ligand-based Schottky diode also outperforms the SCN and TBAI Schottky diodes unintentionally fabricated previously ($SR_{SCN} = 1.4 \times 10^{-4}$, $SR_{TBAI} \approx 0$).

The reduction in dark current observed in the Schottky diode should translate to a reduction in the current noise. Figure 4(c) shows the current noise spectral density comparison of the photoconductor and the Schottky diode. At 15 Hz, our responsivity measurement frequency, the Schottky diode exhibited 1.34×10^{-10} A·Hz$^{-1/2}$ of current noise compared to 8.47×10^{-9} A·Hz$^{-1/2}$ of a photoconductor, which is about a 60-fold reduction. A close examination of the current noise spectra as a function of frequency shows that it follows an inverse power law with an exponent of 0.73, indicating that 1/f is the dominant source of noise. In Figure 4(c), calculated shot noise obtained using the equation $i_n^{shot} = \sqrt{2qI_{dark}}$, where q is the fundamental charge and I_{dark} is the device dark current, and calculated Johnson noise using equation $i_n^{Johnson} = \sqrt{4kT/R}$, where k is the Boltzmann constant, T is the temperature, and R is the device DC resistance, are also overlaid. While in single crystalline devices, other noise mechanisms, such as shot noise or Johnson noise, are often the dominant noise mechanisms, in CQD devices, 1/f noise shows a dominant contribution over a wide range of frequencies [15, 31] and is consistent with this data (1/f knee exceeding 10 KHz). This 1/f noise has been studied to originate from the granular nature of the material and is independent of the chemical composition of the CQD material; metal, semiconductor, and wide-bandgap insulator CQDs all show the similar 1/f noise behavior [16, 32].

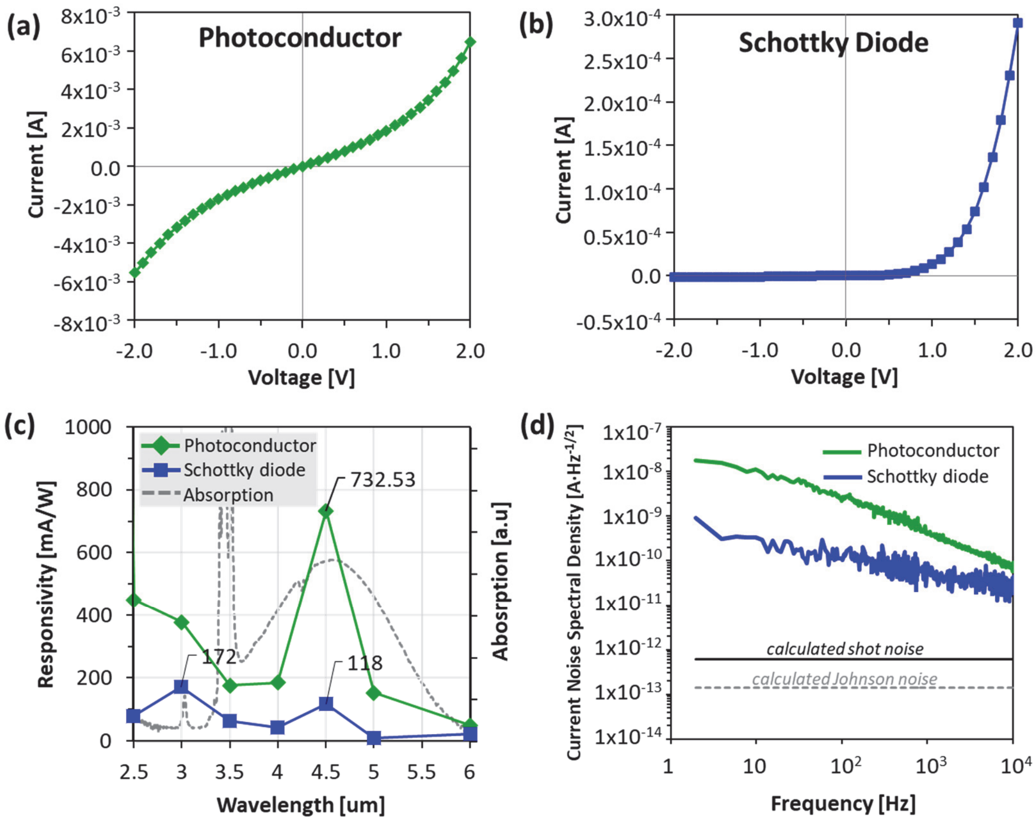

Figure 4. Current-voltage plot of (a) Au-EDT CQD-Au photoconductor and (b) Al-EDT CQD-Au Schottky diode. (c) shows the spectral responsivity comparison. The optical absorption spectrum of Ag_2Se CQD is overlaid for reference. (d) shows the current noise spectral density as a function of frequency. Calculated shot noise and Johnson noise shot noise (6.18×10^{-13} $A \cdot Hz^{-1/2}$) and Johnson noise current (1.40×10^{-13} $A \cdot Hz^{-1/2}$) are overlaid as a reference to the Schottky diode data.

The ultimate figure of merit of a photodetector is the specific detectivity (D^*). Based on the responsivity and current noise measured above, the room temperature D^* of our binary CQD Schottky diode is calculated to be 1.5×10^7 Jones ($cm \cdot Hz^{1/2}/W$) at its 4.5 µm peak. The comparison of detector performance parameters with other technologies (commercial product and leading research) is summarized in Table 1. The current leading-research is based on HgTe CQD p-n junction devices [REF] [33], where the peak responsivity is about 2–3 times lower but shows 10^2-times better noise performance and the D^* is about one order of magnitude higher. Commercial epitaxial HgCdTe (Thorlab VL5T0) [34] is the most mature technology and currently outperforms all CQD technologies, but it suffers from expensive material growth and high cost of focal plane array fabrication. It is also worth noting that the epitaxial HgCdTe and HgTe CQD devices were optically enhanced while our Schottky diode devices have no optical enhancement implemented.

Overall, the binary CQD Schottky diode devices studied in this work show approximately 10^7 Jones of detectivity at room temperature. While the infrared responsivity compares favorably with other technologies, its main limitation is the high current noise arising from 1/f source.

Table 1. Comparison of room temperature device performance parameters of binary CQD Schottky diode (this work) with commercial and leading research photovoltaic technologies. PV stands for photovoltaic.

Detector Material	**Device Type**	**Temp.**	**Peak λ**	**Peak R**	**Current Noise**	**Detectivity at peak**	**Note**
HgTe CQD [REF][33]	PV (p-n junction)	300 K	3.8 µm	0.05 A/W	3.5×10^{-12} $A{\cdot}Hz^{-1/2}$ * (device area $2{\times}10^{-4}$ cm^2)	2.0×10^8 Jones	Optical spacer enhancement
Epitaxial HgCdTe [REF][34]	PV (Thorlab VL5T0)	300 K	5 µm	> 1 A/W	6.6×10^{-12} $A{\cdot}Hz^{-1/2}$ * (device area $1{\times}10^{-2}$ cm^2)	1.5×10^{10} Jones	Optically immersed lens (hyper-hemi spherical GaAs)
Binary CQD (this work)	PV (Schottky diode)	300 K	3 µm, 4.5 µm	0.17 A/W, 0.11 A/W	1.34×10^{-10} $A{\cdot}Hz^{-1/2}$ (device area $4{\times}10^{-4+}$ cm^2)	2.5×10^7 Jones, 1.5×10^7 Jones	No optical enhancements

** The current noise values for epitaxial HgCdTe and HgTe CQD were estimated from the detectivity and responsivity values.*

The low-temperature behavior of our devices has yet to be studied. In the QD photovoltaic device research, cooling has been studied to improve both the responsivity and current noise. Specifically, cooling from 300 K to 100 K leads to an 8-times improvement in the responsivity (from 0.05 A/W to 0.42 A/W) and causes two orders of magnitude reduction in the current noise (from 3.5×10^{-12} $A{\cdot}Hz^{-1/2}$ to 5.9×10^{-14} $A{\cdot}Hz^{-1/2}$), ultimately resulting in a 10^3-times increase in specific detectivity (from 2.0×10^8 Jones to 1.0×10^{11} Jones) [19, 33]. If our binary CQD Schottky device exhibit similar improvements, this will lead to $> 10^{10}$ Jones at $\approx$ 100K. In fact, we anticipate higher performance gains through cooling, because the major constituent of our binary CQD is PbS CQDs and the energy gap of PbS CQD (1.12 eV) is much larger than HgTe CQD~~s~~ (0.25 eV).

CONCLUSION

In summary, we demonstrate MWIR Schottky photodiodes based on binary CQD film composed of intraband Ag_2Se CQDs and PbS CQDs. Among the various capping ligands studied, EDT shows the high infrared responsivity and the introduction of a Schottky barrier using Al contact suppresses the current noise down by an order of magnitude, leading to a detectivity D^* of 10^7 Jones at room temperature.

Along with the cooling discussed previously, further materials and device research can be conducted to improve the performance. In CQD solar cell research, it has been demonstrated that the use of hybrid ligands [REF] [35–37] improves both the CQD film mobility and surface passivation. It is anticipated that a similar strategy can be implemented to MWIR CQD detectors. In a device perspective, the current Schottky diode can be further improved by inserting a thin passivation layer between the metal and CQD layer (known as metal-insulator-semiconductor or MIS device) [20, 38]. Suppression of dark current and current noise is anticipated which may lead to higher detectivity.

METHODS

Chemicals.

Selenium (Se; Sigma-Aldrich, 99.999%), silver chloride (AgCl; Sigma-Aldrich, 99%), oleylamine (OLA; Sigma-Aldrich, 70%), trioctylphospine (TOP; Sigma-Aldrich, 90%), diphenylphosphine(DPP; Sigma-Aldrich, 98%), lead oxide (PbO; Sigma-Aldrich, 99.999%), hexamethyldisilathiane (TMS2S; Sigma-Aldrich, synthesis grade), oleic acid (OA; Sigma-Aldrich, 90%), 1-octadecene (ODE; Sigma-Aldrich, 90%), 1-butanol (Sigma-Aldrich 99.8%), hexane (Sigma-Aldrich, 98.5%), methanol (99.8%), octane (Sigma-Aldrich, 99%), ethyl alcohol (Sigma-Aldrich 99.5%), Acetonitrile (Thermo Scientific 99.5%), 1,2-ethanedithiol (EDT; Fluka, 98.0%), ammonium thiocyanate(NH_4SCN; Sigma-Aldrich, 97.5%), 3-mercaptopropionic acid (MPA; Sigma-Aldrich, 99%), tetrabutylammonium iodide (TBAI; Sigma-Aldrich, 99%) and 1,3 -benzenedithiol (BDT; Sigma-Aldrich, 99%) were used as received.

Ag2Se QD Synthesis.

Ag_2Se QDs having an absorption peak around 4.5 μm were synthesized by following the previously reported standard hot-injection technique [18, 39]. In a glovebox filled with nitrogen, 1 M TOP-Se and 0.5M TOP-Ag precursor solutions were prepared separately by dissolving Se and AgCl in trioctylphosphine (purity 90%). After that, under vacuum, 30 mL of oleylamine was heated to 90 °C in a three-neck flask for 1h. Next, switching the atmosphere to nitrogen, 8 mL of 1 M TOP−Se was injected, and the temperature was raised to 135 °C. When the temperature reached 135 °C, 16 mL of 0.5 M TOP−Ag mixed with 800 μL DPP was injected to initiate a reaction. To terminate the reaction after 20s, 20ml of butanol was injected to the mixture, which is subsequently cooled in a water bath to room temperature. The products were mixed with methanol and ethanol through centrifugation and the precipitate was dispersed in octane after three methanol washes. The solution was then filtered through a 0.45 µm PTFE syringe filter and stored in a vial for further use.

PbS QD Synthesis.

The synthesis of PbS QD with an absorption peak around 1000nm was performed based on the previously developed protocol [40, 41] First, in a three-neck flask a mixture of 0.45 g of lead oxide, 10 mL of 1-octadecene, and 2 mL of oleic acid was mixed and heated under vacuum to 110 °C for 2 h. In a separate vial, the sulfur precursor solution was prepared by mixing 0.2 mL of hexamethyldisilathiane and 5 mL of anhydrous 1-octadecene. This precursor solution was then quickly injected into the reaction flask under a nitrogen environment at 110 °C. As a result, the mixture instantly turned from clear to dark, indicating rapid nucleation. The reaction mixture was then cooled down naturally. Finally, the QDs were precipitated using acetone by centrifuging inside a nitrogen filled glovebox and the final QDs were redispersed in a mixture of hexane.

Device Fabrication.

Devices were fabricated on glass substrates (10 × 10 mm) after cleaning them by sonicating with isopropyl alcohol, acetone, and hexane. After drying the substrates with N_2 flow, 40nm bottom contacts (Cr/Au or Cr/Al) were deposited with thermal evaporation using a shadow mask with a deposition rate around1 Å/s under a vacuum of 2×10^{-6} mbar. By mixing the desired amount of Ag_2Se and PbS solution and stirring it with a vortex machine for 60 s the binary CQDs solution was prepared. The solution was then deposited via spin coating at 2000 rpm for 30s layer by layer (up to 8layers) on the glass substrate with bottom contact. After each layer the substrate was dipped into the desired ligand exchange solution for 20s and rinsed with acetonitrile for 20s. Acetonitrile was used as the solvent for preparing the ligands exchange solutions, the concentrations were as follows, 1,2-ethanedithiol (EDT) 10mM, ammonium thiocyanate (for SCN) 100mM, 3-mercaptopropionic acid 50mM, tetrabutylammonium iodide (TBAI) 10mg/ml, and 1,3 -benzenedithiol (BDT) 1.7mM. After the film deposition, a top contact (Au-70nm) was deposited using a shadow mask through thermal evaporation defining a 200um×200um device area. The fabrication was completed by cleaning the QDs near the bottom contact to expose the contact pad using a wooden tip.

Device Characterization: Device characterizations were carried out using a calibrated blackbody (900 °C, Newport 67030) as an illumination source. The light was modulated using an optical chopper at 15 Hz and filtered through a 4.5 µm band pass filter. The photocurrent was measured using a lock-in technique with SR570 preamplifier and SR 830 lock-in amplifier. The preamplifier also provided the bias to the device. The responsivity (mA/W) was calculated by dividing the measured photocurrent (mA) by the optical power calculated for the 4.5 μm filter (0.65 μW, after correcting for source aperture, optical pass, optics, and detector area). All measurements were done at room temperature without cooling. The device dark resistance was calculated from the current-voltage (I-V) characteristics that were measured using Agilent 4155A semiconductor parameter analyzer.

Dark current noise was measured at 300K using an SR570 preamplifier to amplify the noise spectrum and was recorded using an SR760 Fast Fourier Transform spectrum analyzer. Bias voltages were applied to the devices using the preamplifier's internal battery and Faraday shielded boxes were used to isolate the external noise sources in the lab environment.

References

[1] Henini, M.; Razeghi, M. Handbook of Infrared Detection Technologies, First Edition, Elsevier, 2002

[2] Rogalski, A. Recent progress in infrared detector technologies. Infrared Physics & Technology, 2011, 54, 136–154

[3] Cryer, M. E.; Halpert J. E. 300 nm Spectral Resolution in the Mid-Infrared with Robust, High Responsivity Flexible Colloidal Quantum Dot Devices at Room Temperature. ACS Photonics 2018, 5, 8, 3009–3015

[4] Qiu, J.; Liu, Y.; Cai, Z.; Phan, Q.; Shi, Z. CdSe:In Mid-infrared transparent conductive films prospering uncooled PbSe/CdSe heterojunction photovoltaic detectors. Mater. Adv., 2022, 3, 1079–1086

[5] Rogalski, A. Graphene-based materials in the infrared and terahertz detector families: a tutorial. Adv. Opt. Photonics. 2019, 2, 314–379

[6] Shawkat, M.S.; Hafiz, S.B.; Islam, M.M.; Mofid, S.A.; Al Mahfuz, M.M.; Biswas, A.; Chung, H.-S.; Okogbue, E.; Ko, T.-J.; Chanda, D.; Roy, T.; Ko, D.-K., Jung, Y. Scalable Van der Waals Two-Dimensional PtTe2 Layers Integrated onto Silicon for Efficient Near-to-Mid Infrared Photodetection. ACS Appl. Mater. Interfaces 2021, 13, 15542−15550

[7] Yan,W.; Shresha, V. R.; Jeangros, Q.; Azar, N. S.; Balendhran, S.; Ballif, C.; Crozier, K.; Bullock, J. Spectrally Selective Mid-Wave Infrared Detection Using Fabry-Perot Cavity Enhanced Black Phosphorus 2D Photodiodes. ACS Nano 2020, 14, 13645−13651

[8] Fang, Y.; Ge, Y.; Wang, C.; Zhang, H. Mid-Infrared Photonics Using 2D Materials: Status and Challenges. Laser Photonics Rev. 2019, 14, 1, 1900098

[9] Rogalski, A.; Martyniuk, P.; Kopytko, M.; Hu, W. Trends in Performance Limits of the HOT Infrared Photodetectors. Appl. Sci. 2021, 11, 501

[10] Melnychuk, C.; Guyot-Sionnest, P. Thermodynamic Limits to HgTe Quantum Dot Infrared Detector Performance. J. Electron. Mater. 2022, 51, 1428–1435

[11] Chen, M.; Shen, G.; Guyot-Sionnest, P. Size Distribution Effects on Mobility and Intraband Gap of HgSe Quantum Dots. J. Phys. Chem, 2020, 124, 29, 16216–16221

[12] Dang, T.H.; Abadie, C.; Khalili, A.; Gréboval, C.; Zhang, H.; Prado, Y.; Xu, X.Z.; Gacemi, D; Descamps-Mandine, A.; Ithurria, S.; Todorov, Y.; Sirtori, C.; Vasanelli, A.; Lhuillier, E. Broadband Enhancement of Mid-Wave Infrared Absorption in a Multi-Resonant Nanocrystal-Based Device. Adv. Opt. Mater. 2022, 10, 9, 2200297

[13] Khalili, A.; Weis,, M.; Mizrahi, G.; Chu, A.; Dang,T.H.; Abadie, C.; Gréboval, C.; Dabard, C.; Prado, Y.; Xu, X.Z.; Péronne, E.; Livache, C; Ithurria, S.; Patriarche, G.; Ramade, J.; Vincent, G.; Boschetto, D.; Lhuillier, E. Guided-Mode Resonator Coupled with Nanocrystal Intraband Absorption. ACS Photonics. 2022, 9, 985−993

[14] Hafiz, S. B.; Scimeca, M. R.; Sahu, A.; Ko, D.-K. Colloidal Quantum Dots for Thermal Infrared Sensing and Imaging. Nano Converg. 2019, 6(1), 1–22

[15] Melnychuk, C.; Guyot-Sionnest, P. Auger Suppression in nType HgSe Colloidal Quantum Dots. ACS Nano. 2019, 13, 10512−10519.

[16] Qiu,J.; Liu, Y.; Cai, Z.; Phan, Q.; Shi, Z. CdSe:In Mid-infrared transparent conductive films prospering uncooled PbSe/CdSe heterojunction photovoltaic detectors. Mater. Adv., 2022, 3, 1079–1086

[17] Hafiz, S. B.; Scimeca, M. R.; Zhao, P.; Paredes, I. J.; Sahu, A.; Ko, D.-K. Silver Selenide Colloidal Quantum Dots for Mid-Wavelength Infrared Photodetection. ACS Appl. Nano Mater. 2019, 2, 1631−1636.

[18] Hafiz, S. B.; Al Mahfuz, M. M.; Ko, D.-K. Vertically Stacked Intraband Quantum Dot Devices for Mid-Wavelength Infrared Photodetection. ACS Appl. Mater. Interfaces. 2021, 13, 937−943

[19] Hafiz, S. B.; Al Mahfuz, M. M.; Lee, S.; Ko, D. -K. Midwavelength Infrared p–n Heterojunction Diodes Based on Intraband Colloidal Quantum Dots. ACS Appl. Mater. Interfaces. 2021, 13(41), 49043–49049.

[20] Luther, J. M.; Law, M.; Song, Q.; Perkins, C. L.; Beard, M. C.; Nozik, A. J. Structural, optical, and electrical properties of self-assembled films of PbSe nanocrystals treated with 1, 2-ethanedithiol. ACS nano. 2008, 2(2), 271–280.

[21] Liu, Y.; Gibbs, M.; Puthussery, J.; Gaik, S.; Ihly, R.; Hillhouse, H. W.; Law, M. Dependence of carrier mobility on nanocrystal size and ligand length in PbSe nanocrystal solids. Nano lett. 2010, 10(5), 1960–1969.

[22] Koleilat, G. I.; Levina, L.; Shukla, H.; Myrskog, S. H.; Hinds, S.; Pattantyus-Abraham, A. G.; Sargent, E. H. Efficient, stable infrared photovoltaics based on solution-cast colloidal quantum dots. ACS nano. 2008, 2(5), 833–840.

[23] Szendrei, K.; Gomulya, W.; Yarema, M.; Heiss, W.; Loi, M. A. PbS nanocrystal solar cells with high efficiency and fill factor. Appl. Phys. Lett.2010, 97(20), 203501.

[24] Maulu, A.; Navarro-Arenas, J.; Rodríguez-Cantó, P. J.; Sánchez-Royo, J. F.; Abargues, R.; Suárez, I.; & Martínez-Pastor, J. P. Charge transport in trap-sensitized infrared PbS quantum-dot-based photoconductors: Pros and cons. Nanomaterials, 20018, 8(9), 677.

[25] Jeong, K.S.; Tang, J.; Liu, H.; Kim, J.; Schaefer, A.W.; Kemp, K.; Levina, L.; Wang, X.; Hoogland, S.; Debnath, R. Brzozowski, L.; Sargent, E.H.; Asbury, J.B. Enhanced Mobility-Lifetime Products in PbS Colloidal Quantum Dot Photovoltaics. ACS Nano. 2012, 6 (1), 89–99

[26] Choi, J-.H.; Fafarman, A.T.; Oh, S.J.; Ko, D.-K.; Kim, D.K.; Diroll, B.T.; Muramoto, S.; Gillen, J.G.; Murray, C.B.; Kagan, C.R.; Bandlike Transport in Strongly Coupled and Doped Quantum Dot Solids: A Route to High-Performance Thin-Film Electronics. Nano Lett. 2012, 12(5), 2631–2638

[27] Tang, J.; Kemp, K.W.; Hoogland, S.; Jeong, K.S.; Liu, H.; Levina, L.; Furukawa, M.; Wang, X.; Debnath, R.; Cha, D.; Chou, K.W.; Fischer, A.; Amassian, A.; Asbury, J.B.; Sargent, E.H. Colloidal-quantum-dot photovoltaics using atomic-ligand passivation. Nat. Mater. 2011, 10, pages765–771

[28] Martinez, B.; Livache, C.; Goubet, N.; Jagtap, A.; Cruguel, H.; Ouerghi, A.; Lacaze, E.; Silly, M.G.; Lhuillier, E. Probing charge carrier dynamics to unveil the role of surface ligands in HgTe narrow band gap nanocrystals. J. Phys. Chem. C. 2018, 122(1), 859–865

[29] Carey, G. H.; Levina, L.; Comin, R.; Voznyy, O.; Sargent, E. H. Record charge carrier diffusion length in colloidal quantum dot solids via mutual dot-to-dot surface passivation. Adv. Mater. 2015, 27(21), 3325–3330

[30] Brown, P. R.; Kim, D.; Lunt, R. R.; Zhao, N.; Bawendi, M. G.; Grossman, J. C.; Bulovic, V. Energy level modification in lead sulfide quantum dot thin films through ligand exchange. ACS nano. 2014 8(6), 5863–5872

[31] De Iacovo, A.; Venettacci, C.; Colace, L.; Scopa, L.; Foglia, S. Noise performance of PbS colloidal quantum dot photodetectors. Appl. Phys. Lett. 2017, 111(21), 211104.

[32] Liu, H.; Lhuillier, E.; Guyot-Sionnest, P. 1/f noise in semiconductor and metal nanocrystal solids. J. Appl. Phys. 2014, 115(15), 154309.

[33] Thorlabs, VL5T0 - HgCdTe Single-Junction Photovoltaic Detector, 5.0 µm, 1 mm^2 Active Area. https://www.thorlabs.com/thorproduct.cfm?partnumber=VL5T0 (accessed July 06, 2022)

[34] Ackerman, M. M.; Tang, X.; Guyot-Sionnest, P. Fast and sensitive colloidal quantum dot mid-wave infrared photodetectors. ACS nano. 2018, 12(7), 7264–7271

[35] Ip, A. H.; Thon, S. M.; Hoogland, S.; Voznyy, O.; Zhitomirsky, D.; Debnath, R.; Levina, L.; Rollny, L.R.; Carey, G.H.; Fischer, A.; Kemp, K.W.; Kramer, I.J.; Ning, Z.; Labelle, A.J.; Chou, K.W.; Amassian, A.; Sargent, E. H. Hybrid passivated colloidal quantum dot solids. Nat. Nanotechnol. 2012, 7(9), 577–582.

[36] Zhang, J.; Gao, J.; Church, C.P.; Miller, E.M.; Luther, J.M.; Klimov, V.I.; Beard, M.C. PbSe Quantum Dot Solar Cells with More than 6% Efficiency Fabricated in Ambient Atmosphere. Nano Letters 2014 14 (10), 6010–6015

[37] Yang, Y.; Zhao, B.; Gao, Y.; Liu, H.; Tian, Y.; Qin, D.; Wu, H.; Huang, W.; Hou, L. Novel hybrid ligands for passivating PbS colloidal quantum dots to enhance the performance of solar cells. Nano-micro lett. 2015, 7(4), 325–331

[38] Lin, C. H.; Liu, C. W. Metal-insulator-semiconductor photodetectors. Sensors 2010 10(10), 8797−8826

[39] Sahu, A.; Khare, A.; Deng, D.; Norris, D. J. Quantum Confinement in Silver Selenide Semiconductor Nanocrystals. Chem. Commun. 2012, 48, 5458−5460

[40] Zhang, J.; Crisp, R. W.; Gao, J.; Kroupa, D. M.; Beard, M. C.; Luther, J. M. Synthetic Conditions for High-Accuracy Size Control of PbS Quantum Dots. J. Phys. Chem. Lett. 2015, 6, 1830−1833.

[41] Hines, M. A.; Scholes, G. D. Colloidal PbS Nanocrystals with Size-Tunable Near-Infrared Emission: Observation of Post-Synthesis Self-Narrowing of the Particle Size Distribution. Adv. Mater. 2003, 15, 1844−1849.